Numerical simulation of the flight of a badminton shuttlecock using the SPH method

Mirantsoa Rasolofomanana, N. Grenier, Christian Tenaud

Noname manuscript No.
(will be inserted by the editor)

Numerical simulation of the flight of a badminton shuttlecock using the SPH method.

Mirantsoa Rasolofomanana · Nicolas Grenier · Christian Tenaud

Received: date / Accepted: date

Abstract This study aims at studying the capability of a meshless method, the Smoothed Particle Hydrodynamics (SPH) method, to predict the whole flight of a badminton shuttlecock, including the first stage of its flight where flipping motion induced by the dynamics or the player occurs. As a first step, our study is restricted to 2D configurations, and a 2D shuttlecock model is proposed that has same dimensions and weight of a real shuttlecock. After first validating the numerical approach on a simple test-case of a ballistic flight of a cylinder, we investigate flights of the proposed 2D shuttlecock model. Similarly to previous numerical studies [10, 11], we simulate the air flow around a shuttlecock fixed in a wind tunnel and find that the variation versus the Reynolds number of the drag coefficient (C_x) is in a quite good agreement with experimental averaged values. We also investigate the badminton shuttlecock trajectory in the most stable configuration where the cock stopper is already in front of the trajectory and show that trajectories are similar to the ones studied in the work of Cohen *et al.* [4]. We finally simulate the complete flight of the badminton shuttlecock, from the departure with the cock stopper oriented backward, to the final stage of the flight with a stable trajectory. We show that the main characteristics of the flight as well as the shuttlecock behavior during the flight can be reproduced thanks to this numerical approach, and we analyze all the phases of the flight: the turning over phase, the oscillation phase, and then the stabilization phase. Numerical results obtained in this

M. Rasolofomanana,
Université Paris-Saclay, CNRS, LIMSI, Orsay, France
E-mail: Mirantsoa-aime.Rasolofomanana@universite-paris-saclay.fr

N. Grenier,
Université Paris-Saclay, CNRS, LIMSI, Orsay, France
E-mail: Nicolas.Grenier@limsi.fr

C. Tenaud,
Université Paris-Saclay, CNRS, LIMSI, Orsay, France
E-mail: Christian.Tenaud@limsi.fr

study compare favorably with previous experimental studies. To the best of our knowledge, it is the first time that the complete flight of a badminton shuttlecock has been numerically predicted.

Keywords Badminton shuttlecock · Navier-Stokes equations · Smoothed Particle Hydrodynamics method

1 Introduction

Badminton is a sport that, unlike other racquet sports, uses a shuttlecock, which is a asymmetric projectile far away from a ball. Conventional badminton shuttlecock usually consists of a cork stopper at the head extended by a conical skirt either of structured plastic-made or of sixteen overlapping feathers. The cork stopper is much heavier than the skirt. The asymmetrical shape of the shuttlecock confers certain aerodynamic properties that are exploited by skilled players while managing to keep the shuttlecock within the authorized limits of the field. For experienced players, the badminton shuttlecock can reach higher speeds than projectiles used in other sports, but it decelerates much faster due to its own drag that changes during the flight. Trajectories of the badminton shuttlecock are very special and do not look like those of an ordinary ball.

To exemplify this we will compare the range of a shuttlecock subjected to drag forces with a projectile without taking into account the aerodynamic force. It is well know that a projectile originally fired in the absence of aerodynamic force follows a parabolic trajectory and its range is given by $d_{scope} = u_0^2 sin2\alpha/g$, where u_0 is the initial velocity at which the projectile is fired, g the acceleration of gravity, and α the departure angle with respect to the horizontal axis (Ox). A ball pulled with a velocity $u_0 = 24.7\,\mathrm{ms}^{-1}$ at an angle $\alpha = 44°$ would then reach a range of up to about 60 meters without taking into account the aerodynamic force while a badminton shuttlecock taking the drag forces into account would only reach a range that is 9 times less important (about 7 meters) [4]. It is worth when the initial velocity increases since for $u_0 = 37.8\,\mathrm{ms}^{-1}$ and a departure angle $\alpha = 38°$, the theoretical range without friction is about 140 meters while only 8 meters for a shuttlecock [4]. Aerodynamics plays a crucial role in the badminton, and It is clear that the drag of a shuttlecock significantly affects its trajectory. In fact, several parameters are at play on the trajectory of a badminton shuttlecock during its flight. We can mainly cite the initial hitting velocity, the shooting angle, the viscosity of air linked to its temperature and its humidity, the mass of the shuttlecock, and the type of shuttlecock (feather or plastic) for the major parameters.

Despite the immense popularity of this game, there are only few studies on the aerodynamic properties of the badminton shuttlecock, unlike other projectiles used in sports. The majority of these studies are experimental. Most of them aim at measuring the drag force of the shuttlecock depending of the shuttlecock characteristics in order to build a law of the drag coefficient versus the Reynolds number [1–5]. Once the drag coefficient law is known, the flight of the

badminton shuttlecock can easily be determined by following the fundamental principle of dynamics using the second Newton's law. Several studies have been devoted to analyze this special trajectory [6,7,3,4], knowing an initial velocity and departure angle. Some studies investigate the role of the spinning around the major axis of the shuttlecock, due to the arrangement of the 16 feathers, to understand the relationship existing between the aerodynamic properties of the shuttlecock and this rotation [8,9]. For the most, these studies are confined to the dominant configuration of the badminton shuttlecock during its flight, which is also the most stable, corresponding to the configuration where the main symmetry axis is aligned with the velocity (of the shuttlecock). Some studies take however into account the influence of the yaw angle on the aerodynamic of the shuttlecock to investigate the modification of the trajectory induced [7,4].

Besides these experimental studies, very few studies based on numerical simulations of the flow in the vicinity of the badminton shuttlecock have been conducted. Computational Fluid Dynamics (CFD) has however been used to study the aerodynamics of a badminton shuttlecock in the most stable configuration, *i.e.* with the major shuttlecock axis aligned with the velocity vector. Verma *et al.* [10] studied through numerical simulations based onto Reynolds Averaged Navier-Stokes (RANS) approach, the influence of the nature of the skirt, either feather or plastic, and the influence of the gap in the skirt on the aerodynamics of a shuttlecock fixed in a uniform flow. It was shown that gaps have a crucial role in the inside/outside pressure difference around the skirt that mainly contributes to the drag. J. Hart [11] investigated the role of the numerical approach, between RANS and Scale Resolving Simulation (SRS, like URANS, DES, LES), on the numerical prediction of the flow around a plastic made badminton shuttlecock fixed in a uniform flow. Only the SRS approaches are able to represent with confidence the time-dependent flow structures around the body, meaning that only time-resolved methods (like SRS or DNS) would be capable of predicting the shuttlecock trajectory.

Nevertheless, it is the action of the racket on the badminton shuttlecock that largely determines the variety of the shuttlecock flights. After the initial impulse given by the racket strings on the cork stopper (cork being turn backward), the shuttlecock flips, the cork moving forward, before it continues its flight. The shuttlecock thus follows a variety of trajectories depending on the type of stroke the experienced player do (spin-in, spin-out, increasing the initial spin, ...). It is therefore not enough to be interested in the flight of the shuttlecock with a zero angle of attack if one wants to accurately predict its trajectory. Experiments have been conducted to exemplify these first stage motion of the shuttlecock [4]. However, to our knowledge, there does not exist, that time, any numerical simulation predicting the whole flight of the badminton shuttlecock from the impact of the racket. The goal of this study is therefore to propose a numerical methodology capable of correctly predicting the flight of a badminton shuttlecock with the flipping motion occurring in the first phase of its flight.

Simulating the flow in the vicinity of the badminton shuttlecock during its flight is a tough challenge since the shuttlecock has a relatively complex geometry that is hard to enmesh (thin structured skirt with holes, thin feathers, ...), with displacements over large extents, and potentially deformations due to fluid-structure interactions. These are reasons that can certainly be put forward to explain why there are really few numerical studies. We could think of using mesh-based numerical approaches with mesh fitting the body as already done in [10,11]. In the context of moving body, Arbitrary Lagrangian Eulerian (ALE) method (see [12,13] for instance) could be adopted to deform the fluid domain in order to follow the movement of the body. However, based on mesh fitting the solid boundaries, the ALE method often involves costly re-meshing of the fluid domain when the solid body undergoes large displacements, mainly with large rotation angles. One alternative could be provided by fictitious domain methods (see [14,15] for instance) that work on a fixed grid; the solid being superimposed on the fluid mesh, special treatments of the equations are used on mesh point embedded in the body to ensure the right solid boundary conditions. Such methods could encompass large displacements without remeshing. However, they struggle to account for very thin solid body because it demands a wide number of points that becomes prohibitive. To overcome these problems, we prefer here to employ a mesh-less approach based on Smoothed Particle Hydrodynamics approach [16]. This method has been largely used in many fields of research, including astrophysics [17], free-surface flows [21], elastic-plastic solids [22], fluid-structure interaction [23,24]. It is a Lagrangian method where particles that transport fluid information move with the fluid. SPH method is mainly applied to various nonlinear phenomena where the absence of a grid becomes interesting to simulate large boundary/interface displacements or deformations, as encountered in free-surface/interfacial flows, solid impact and explosion simulations or fluid-structure coupling. In fact, large ballistic displacements and non-linear flows around moving projectiles with complex geometry that undergo large displacements justify the choice of the SPH method.

This study aims at studying the capability of the SPH method to predict the whole flight of a badminton shuttlecock, including the first stage of its flight where flipping motion occurs. To the best of our knowledge, it is the first time that the complete flight of a badminton shuttlecock has been numerically predicted. As a first step, we restrict our study to 2D configurations, and a 2D shuttlecock model is proposed in this study.

We first present, in section § 2, the SPH method without going into details. We stress its application to the equations of fluid mechanics we have to solve and describe the discretized equations obtained and its numerical resolution. A 2D model of badminton shuttlecock has then been proposed in section § 3 that has same dimensions and weight of a real shuttlecock. As gaps in the skirt have an important effect [11], a special attention is payed to take these artifacts into account in the 2D model. Equations of the the solid body motion are then presented with the translational motion of its center of mass and the rotational motion around its center of mass. We explain how to calculate the center of

mass and the moment of inertia for our proposed 2D shuttlecock model. Before simulating the flight of the badminton shuttlecock, we first validate, in section § 4, the numerical approach based on the SPH approach on a simple test-case of a ballistic flight of a cylinder and compare numerical results to reference solutions. In the last section (§ 5), we investigate the flight of the proposed model of a badminton shuttlecock. Similarly to previous numerical studies [10, 11], we simulate the air flow around a shuttlecock fixed in a wind tunnel and discuss the variation of the drag coefficient (C_x) versus the Reynolds number. We then investigate the badminton shuttlecock trajectory in the most stable configuration where the cock stopper is already in the front of the trajectory. We finally simulate the complete flight of the badminton shuttlecock, from the departure with the cock stopper oriented backward, to the final stage of the flight with a stable trajectory and analyze all the phases of the flight. We then conclude (§ 6) this study and address some perspectives to this original work.

2 Numerical method

As we are interested in the flight of a badminton shuttlecock in a fluid domain, we are therefore facing a problem of fluid-structure interaction with large displacement of the solid. The fluid-structure interaction concerns the study of the behavior of a system composed of two parts: a mobile solid structure (that could either be rigid or deformable) and a fluid (flowing or at rest) around or inside the structure. In our study, for simplicity in a first approach, we consider a solid with no deformation of the structure and the fluid is initially at rest. Motions of the fluid and the solid are strongly coupled: the motion of the solid results from both its own inertia and the external forces exerted by the fluid onto the external surface of the solid; the fluid is therefore strongly affected by the action of the solid by displacements of mass and momentum.

The fluid motion is governed by the weakly compressible Navier-Stokes equations. As the solid body is subjected to displacements over large extents, a meshless approach based on Smoothed Particle Hydrodynamics (SPH) approach is the method adopted throughout this study. In this section, we will first present the equations of the fluid motion. We will then present the SPH method without going into details and its application to the weakly compressible Navier-Stokes equations. At last, we will describe the motion of the solid subjected to external forces and will end up with the coupling procedure.

2.1 Equations of the fluid motion:

The fluid we are studying is supposed newtonian, and weakly compressible. The continuous fluid domain is then discretized by material fluid particles that carry the fluid information (position, velocity, pressure, volume of particles). The SPH method follows particles in their mouvement, and the equations of

motion reflect the conservation of mass and momentum and the Lagrange character of the flow. Written in a Lagrangian form the Navier-Stokes equations read:

- mass conservation:
$$\frac{D\rho}{Dt} + \rho\boldsymbol{\nabla}\cdot\mathbf{u} = 0, \tag{1}$$
- momentum conservation:
$$\frac{D\mathbf{u}}{Dt} = -\frac{\boldsymbol{\nabla}p}{\rho} + \frac{\boldsymbol{\nabla}\mathcal{T}}{\rho} + \mathbf{g}, \tag{2}$$
with $\dfrac{\boldsymbol{\nabla}\mathcal{T}}{\rho} = \dfrac{\mu}{\rho}\Delta\mathbf{u}$ by assuming weak effects of compressibility, μ is the dynamic viscosity of the fluid,
- Lagrangian character of the flow (velocity):
$$\frac{d\mathbf{x}}{dt} = \mathbf{u}. \tag{3}$$

Let us recall that the total derivative is given by $\dfrac{Df}{Dt} = \dfrac{\partial f}{\partial t} + \dfrac{d\mathbf{x}}{dt}\cdot\boldsymbol{\nabla}f = \dfrac{\partial f}{\partial t} + \mathbf{u}\cdot\boldsymbol{\nabla}f$.

To close this system of equations we need to relate the pressure (p) to the independent variables of the problem. The modified Tait's equation of state [27] that relates the pressure (p) to the density (ρ), assuming an isentropic transformation, is commonly used in SPH method:

$$p = p_0 + \frac{\rho_0 c_0^2}{\gamma}\left[\left(\frac{\rho}{\rho_0}\right)^{\gamma} - 1\right], \tag{4}$$

where γ is the specific heat capacity ratio (also called Laplace coefficient), c_0 is the pseudo-speed of sound, ρ_0 and p_0 are respectively the reference density and the reference pressure.

The choice of the speed of sound is purely artificial since we want to avoid numerical difficulties associated with real speed of sound (propagation of acoustic perturbations, time-step restrictions and excessive numerical dissipation) as well as solving incompressible equations (where speed of sound is infinite) to avoid computationally expensive linear system resolution.

In the present study, the compressibility effect is considered as very weak since the largest shuttlecock velocity we have considered (less than $70\,\mathrm{ms}^{-1}$) is very far away from the speed of sound ($340\,\mathrm{ms}^{-1}$ at a temperature of $20\,^{\circ}\mathrm{C}$). We easily assume that the acoustic waves have neither influence on the shuttlecock flight nor on the flow around the shuttlecock. For this reason, we choose a weakly compressible approach that consider small relative density variations ($\delta\rho/\rho_0 \simeq 1\% \ll 1$).

To link this constraint on density variations to speed of sound, we consider the adiabatic velocity of sound as constant:

$$c_0^2 = \frac{\delta p}{\delta\rho}, \tag{5}$$

where δp denotes the variations of the pressure of the fluid. By considering that variations of pressure are mainly attributed to variations of the dynamical pressure (i.e. $\delta p \sim \rho_0 {u_0}^2$, u_0 being the reference velocity), the sound celerity could be express as:

$$c_0^2 \simeq \frac{\rho_0 {u_0}^2}{\delta\rho}.$$

Following the assumption made on the small variation of the density, this gives us:

$$\frac{u_0^2}{c_0^2} \simeq 1\% \Longleftrightarrow Ma = \frac{u_0}{c_0} = 0.1. \tag{6}$$

To fulfill this constraint on Mach number Ma, the artificial speed of sound must be chosen ten times greater than the reference velocity (u_0), characteristic of the flow in each study.

2.2 The Smoothed Particle Hydrodynamics (SPH) method

The SPH method is based on a so-called integral representation of a function. Considering a closed domain Ω with $\partial\Omega$ its boundary, the value of a function f at a point $\mathbf{x}$ of Ω can be written:

$$f(\mathbf{x}) = \int_\Omega f(\mathbf{x'})\delta(\mathbf{x} - \mathbf{x'})d\mathbf{x'},$$

where δ is the Dirac function. As the Dirac function is not everywhere differentiable, it is approximate by a function called kernel whose extension is related to a smoothing length (h). Then, the approximation of the function $f(\mathbf{x})$ in Ω can be written as:

$$f(\mathbf{x}) \approx < f(\mathbf{x}) >^h = \int_\Omega f(\mathbf{x'})W(\mathbf{x} - \mathbf{x'}, h)d\mathbf{x'}, \tag{7}$$

where $W(\mathbf{x} - \mathbf{x'}, h)$ is the kernel function. When h tends to zero, the kernel function tends to a Dirac distribution and we therefore obtain:

$$\lim_{h\to 0} W(\mathbf{x} - \mathbf{x'}, h) = \delta(\mathbf{x} - \mathbf{x'}). \tag{8}$$

The kernel function must then satisfy some properties, *i.e.* must be positive, decrease monotonously, satisfy the partition of unity:

$$\int_\Omega W(\mathbf{x} - \mathbf{x'}, h)d\mathbf{x'} = 1, \tag{9}$$

and its gradient must be zero:

$$\int_\Omega \boldsymbol{\nabla} W(\mathbf{x'} - \mathbf{x}, h)d\mathbf{x} = 0. \tag{10}$$

This gradient must also respects the antisymmetry property:

$$\boldsymbol{\nabla} W(\mathbf{r}, h) = -\boldsymbol{\nabla} W(-\mathbf{r}, h).$$

Theoretically, any function that satisfies the above conditions can be used as a kernel function. Since kernel values fall rapidly to zero for increasing radius, hypothesis of compact support on a sub-space Ω_i of Ω is also made: the kernel recovers non-zero values inside the sub-space Ω_i and zero outside. Extend of this support is defined with respect to h and is commonly of order $2h$ or $3h$. Various types of functions, especially Gaussian function or piecewise polynomials (splines) have been tested. Despite their accuracy, Gaussian function is not used in practise due to its expensive computational cost. An exemple of a kernel function is given on figure 1 for one and two space dimensions.

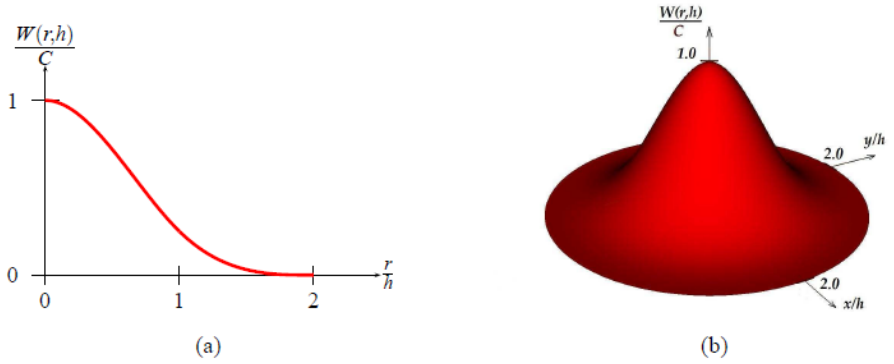

Fig. 1 Kernel functions in 1D (on the left) and 2D (on the right) - Figures are taken from [18].

2.3 Numerical approximation of the Navier-Stokes equations:

Sub-spaces Ω_i are defined by their barycentre P_i. Due to compact support of the kernel, neighbourhood of point P_i can be defined as the set D of sub-spaces Ω_j for which barycentre P_j belongs to kernel support of point P_i. To approximate integrals the following quadrature is used:

$$\int_{\Omega_i} f(\mathbf{x}) d\mathbf{x} \simeq \sum_{j \in D} f(\mathbf{x_j}) \omega_j, \tag{11}$$

where ω_j is the elementary volume of sub-space Ω_j. The convolution (7) of the function f then becomes:

$$< f(\mathbf{x_i}) >^h = \sum_{j \in D} f(\mathbf{x_j}) W(\mathbf{x_i} - \mathbf{x_j}, h) \omega_j. \tag{12}$$

When applying convolution approximation (7) to gradient of f, we obtain:

$$\boldsymbol{\nabla} f(\mathbf{x}) \approx < \boldsymbol{\nabla} f(\mathbf{x}) >^h = \int_\Omega \boldsymbol{\nabla} f(\mathbf{x'}) W(\mathbf{x} - \mathbf{x'}, h) d\mathbf{x'}. \tag{13}$$

By integrating by parts and applying the Green-Ostrogradski theorem, we get:

$$< \boldsymbol{\nabla} f(\mathbf{x}) >^h = \int_{\partial\Omega} f(\mathbf{x'}) W(\mathbf{x} - \mathbf{x'}, h) \mathbf{n} dS - \int_\Omega f(\mathbf{x'}) \boldsymbol{\nabla} W(\mathbf{x} - \mathbf{x'}, h) d\mathbf{x'}, \tag{14}$$

with $\mathbf{n}$ the normal unit vector at the boundary surface $\partial\Omega$ of the domain Ω. When the kernel compact support does not intersect the boundary $\partial\Omega$, we can neglect boundary surface $\partial\Omega$ contribution and we obtain:

$$< \boldsymbol{\nabla} f(\mathbf{x}) >^h = - \int_\Omega f(\mathbf{x'}) \boldsymbol{\nabla} W(\mathbf{x} - \mathbf{x'}, h) d\mathbf{x'}.$$

As we suppose the antisymmetric property of the gradient ($\boldsymbol{\nabla} W(\mathbf{r}, h) = -\boldsymbol{\nabla} W(-\mathbf{r}, h)$), the discretized form of the gradient of the function f is:

$$< \boldsymbol{\nabla} f(\mathbf{x_i}) >^h = \sum_{j \in D} f(\mathbf{x_j}) \boldsymbol{\nabla} W(\mathbf{x_j} - \mathbf{x_i}) \omega_j. \tag{15}$$

The basis of the method and the discrete approximations presented in the previous section are then applied to the equations of fluid motion. The discretization of conservation equations (1, 2) with previous relations (12, 15) leads to non-consistent approximations of these equations and are subject to numerical instabilities. To derive consistent and stable numerical scheme, we invite the reader to refer to [26,25]. SPH scheme writes finally:

– mass conservation:

$$\frac{D\rho_i}{Dt} = -\rho_i \sum_{j \in D} (\mathbf{u_j} - \mathbf{u_i}) \boldsymbol{\nabla} W_{ij} \omega_j \tag{16}$$

– momentum conservation:

$$\frac{D\mathbf{u_i}}{Dt} = -\frac{1}{\rho_i} \sum_{j \in D} (p_j + p_i) \boldsymbol{\nabla} W_{ij} \omega_j - \sum_{j \in D} \frac{2\mu}{\rho_i} (\mathbf{u_i} - \mathbf{u_j}) \frac{(\mathbf{x_i} - \mathbf{x_j}) \boldsymbol{\nabla} W_{ij}}{\|\mathbf{x_i} - \mathbf{x_j}\|^2} \omega_j + \mathbf{g} \tag{17}$$

– particle motion:

$$\frac{d\mathbf{x_i}}{dt} = \mathbf{u_i} \tag{18}$$

where the following notations are employed: $f_i = f(x_i)$ and $W_{ij} = W(\mathbf{x_i} - \mathbf{x_j}, h)$,

2.4 Numerical resolution of the fluid motion:

To evolve in time this system of equations (16)-(18), explicit time forwarding scheme is employed, such as 4^{th}-order Runge-Kutta (with Courant-Friedrichs-Lewy constant usually equal to 0.3). However combining such explicit scheme with spatially-centred discretization is unconditional stable and may not be usable. Classical workarounds are to introduce artificial viscosity [16] to dissipate numerical perturbation or to interpret SPH scheme as an ALE scheme [26] to recover results of discretization of hyperbolic system of conservation laws. In such framework, SPH scheme is of Godunov-type and classical exact (or approximate) Riemann solver can be applied to stabilize the scheme. Due to superior accuracy and no tunable parameter, we choose this Godunov approach.

Due to Lagrangian nature of this meshless method, prescription of accurate and robust boundary conditions is not straightforward. Difficulties come also from the compact support of the SPH convolution operator which becomes incomplete when overlapping a boundary. Two approaches exist to circumvent these difficulties. The first one consists of mirroring flow with respect to boundary with ghost particles to complete compact support [25]. However this technique suffers from some inaccuracies when boundary geometry exhibits singularities (corners, ...) or curvature. The second approach, as in classical mesh-based method, is to discretize boundaries to apply appropriate conditions. After first inconsistent attempts by imposing repulsive potentials on fixed wall particles [21], more accurate methods were derived by considering the discretization of the complete gradient operator (14). This class of renormalization methods [29] is more robust when dealing with complex geometry and is selected to impose boundary conditions of present study. Unless specified, no-slip condition is prescribed ($\mathbf{u} = \mathbf{0}$) on walls.

2.5 Motion of the solid subjected to external forces:

The movement of the rigid body can be decomposed into a translational motion of its center of mass and a rotational motion around its center of mass. The translational movement is described by following equations on position and velocity:

$$\frac{d\mathbf{r_G}(t)}{dt} = \mathbf{u_G}(t), \quad M\frac{d\mathbf{u_G}(t)}{dt} = M\mathbf{g} + \mathbf{F_G^{ext}}, \tag{19}$$

where $\mathbf{r_G}(t) = (x_{\mathbf{r_G}}(t), y_{\mathbf{r_G}}(t))$ is the position at time t of the center of mass, $\mathbf{u_G}$ its velocity, M the mass of the solid and $\mathbf{F_G^{ext}}$ are external forces applied onto the object (either applied on his surface or with a volumetric force).

The rotational movement is described by equations which involve the moment of inertia:

$$\frac{d\mathbf{\Theta}(t)}{dt} = \omega(t), \quad I_G\frac{d\omega(\mathbf{t})}{dt} = \mathcal{M}_{\mathbf{F^{ext}}/G} = \mathbf{GP} \wedge \mathbf{F_G^{ext}}, \tag{20}$$

where $\Theta(t)$ is the angular position, $\omega(t)$ the angular velocity, I_G the inertia matrix with respect to the center of mass (G) and $\mathcal{M}_{\mathbf{F^{ext}}/G}$ the moment of external forces $\mathbf{F_G^{ext}}$ applied to the point P with respect to (G). To ease the reading of this paper, calculations of the center of mass and the inertia matrix for the proposed model of the shuttlecock are given in the appendix sections § A.1, and A.2, respectively.

2.6 Coupling procedure between fluid and rigid solid:

To simulate the interaction between fluid flow and freely moving rigid body, one must take care of three major parts: the fluid flow model already detailed, the movement of the rigid body previously presented as well as the coupling between fluid and solid models. This latter two-way coupling consists of two simultaneous effects. First, the displacement of the rigid body generates a deformation of fluid domain boundaries and as a result of the whole fluid domain. Since the SPH discretization is by-nature meshless and Lagrangian, this displacement constraint is straightforward in this particle-based numerical framework. Conversely, the reaction of the fluid flow on the rigid body manifests locally by fluid constraints applied on boundaries of the solid: the aerodynamic forces applied on the body surface. Since the body is considered as rigid, these fluid constraints (see [28] for details) can be integrate on its boundaries to result into forces ($\mathbf{F_G^{ext}}$) and moments ($\mathbf{r} \wedge \mathbf{F^{ext}}$) which will modify momentum (equation (19) and angular momentum conservation of the solid (equation 20).

All previous numerical models and considerations are implemented in the `SPH-flow` software (version 18.12.1, edited by Nextflow Software) which have been used for the present study.

3 A proposed 2D model of the shuttlecock

The badminton shuttlecock is of course an important element of this sport. There are mainly two types of shuttlecock (see figure 2): the plastic shuttlecock, mainly used by beginners because of its low cost and its robustness, and the feather shuttlecock much used by competitors because of its trajectory fineness and the playing pleasure it brings.

The badminton shuttlecock consists mainly of a cork followed by a skirt. As already said, the present study is restricted to 2D simulations as a proof of concept. Therefore, we define a 2D model of a shuttlecock. The cork is then considered as a half-disc followed by a rectangular part and the skirt is a discontinuous trapezoid (as one can see on figure 3). The proposed 2D model respects characteristics of a real shuttlecock in terms of masses and dimensions. Following [9], dimensions and mass of each part of the 2D model are reported in table 1.

Fig. 2 Example of badminton shuttlecocks (plastic version, on the left, and made with feathers, on the right).

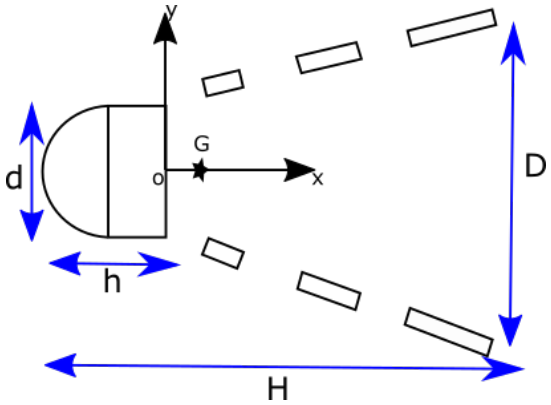

Fig. 3 A proposed 2D model of a shuttlecock. Center of reference at the center of the backward face of the cork.

Total length (H)	Skirt length (L)	Cork length (h)	Skirt width (D)	Cork width (d)	Total mass (M)	Mass of the cork (m_{cork})	Mass of the skirt (m_{skirt})
85 mm	60 mm	25 mm	66 mm	26.4 mm	5.4 g	3.2 g	2.2 g

Table 1 Dimensions of the shuttlecock model and mass of each part.

4 Validation of the numerical tool on the trajectory of a cylinder in a ballistic flight.

Before simulating the flight of a shuttlecock, it is necessary to first validate the numerical approach used in `SPH-flow` by simulating simple test-cases

of projectile flight and validating numerical results compared to theoretical solutions.

The ballistic flight of a cylinder, with a spanwise length of unity ($H = 1\,\mathrm{m}$), is first considered in air initially at rest. As sketched in figure 4, a unit length cylinder (treated as a disc in 2D of diameter $D = 13.2\,\mathrm{mm}$ and mass $m = 1\,\mathrm{kg}$) is shot with an initial velocity $u_0 = 4.118\,\mathrm{ms}^{-1}$ at an angle $\alpha = 72.3°$ relatively to the horizontal axis (Ox).

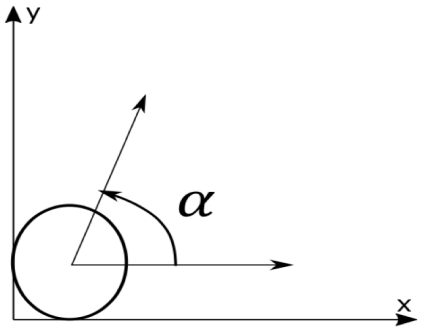

Fig. 4 Sketch of the initial state of the ballistic fligth of a cylinder shot in air at an initial velocity $\mathbf{u}_0$ with an angle α relatively to the horizontal axis (Ox).

The fluid has following properties: dynamic viscosity $\mu = 1.77 \times 10^{-5}\,\mathrm{Pa\,s}$ and density $\rho = 1.2\,\mathrm{kg\,m}^{-3}$. The acceleration of gravity g is equal to $9.81\,\mathrm{m\,s}^{-2}$.

If we consider the unit length cylinder subjected to its own weight, the equation of its trajectory in the laboratory frame (O, x, y) is then given by:

$$y(x) = \frac{g}{2}\left(\frac{x - x_0}{u_{0x}}\right)^2 + u_{0y}\left(\frac{x - x_0}{u_{0x}}\right) + y_0 \tag{21}$$

where (x_0, y_0) are the coordinates of the initial location of the disc center, and u_{0x}, u_{0y} components of the initial velocity vector $\mathbf{u}_0$. This equation gives the classical parabolic type trajectory with a distance range of $d_{scope} = u_0^2 sin2\alpha/g$.

However, following this simple assumption, this equation is far from giving a real trajectory in air because, as it is well known for sufficiently high velocity magnitude, aerodynamic forces greatly affect the body trajectory and these forces must be taken into account in the derivation of the motion equation. Aerodynamic forces can be shared between a *drag force* that is exerted on the solid body, aligned with the body displacement but in the opposite direction, and *lift* and *crosswind* forces that are perpendicular to the body displacement, the *lift* force being directed in the vertical direction while the *crosswind* force in the spanwise direction. Restricted to the 2D framework, only the *drag* and the *lift* forces are here considered.

Considering the present disc flight, the flow in the vicinity of the disc can be considered in a turbulent regime since the Reynolds number, defined as

$Re_D = \rho u_0 D/\mu$, is in-between 2.2×10^3 and 1.1×10^4. Let us recall that the Reynolds number (Re) is a dimensionless number that measures the importance of forces of inertia compared with viscous forces; the more the flow inertia, the greater the Reynolds number, and the less viscous the fluid the greater Re. In the turbulent flow regime, the friction forces acting at the cylinder wall are proportional to the square of the velocity [7]. Consequently, the drag force model is defined as follows:

$$\mathbf{F}_{drag} = \frac{1}{2}\rho S C_x u.\mathbf{u}, \tag{22}$$

with S the reference surface which is generally taken as the front surface in aerodynamic studies, let say: $S = DH$ (where $H = 1\,\text{m}$ in 2D), u the velocity magnitude of the body, and ρ the density of the fluid. C_x is the drag coefficient which depends on the solid body considered. This drag coefficient mainly depends on the Reynolds number. Considering a smooth cylinder or a smooth sphere in an air flow, the variation of the drag coefficient versus the Reynolds number is well documented in literature (see [19]).

Regarding the lift force, it will be neglected in this theoretical development because it remains very weak compared with the drag force since the object considered is symmetric and the flow stays almost symmetric in average.

Considering now that the disc is subjected to its own weight and the drag force, the *fundamental principle of dynamics*, *i.e.* the second Newton's law, gives:

$$m\frac{d\mathbf{u}}{dt} = m\mathbf{g} - \frac{1}{2}\rho S C_x u.\mathbf{u}. \tag{23}$$

To recover the time variations of the velocity and the center of mass location of the disc, we numerically integrate equation (23) in time. Setting $\beta = \frac{1}{2}\rho S C_x$, and applying a first order explicit time discretization, we get the time variation of the velocity in the plane (O, x, y):

$$\begin{cases} u_x^{n+1} - u_x^n = -\beta\frac{\delta t}{m}\left(\sqrt{(u_x^n)^2 + (u_y^n)^2}\right)u_x^n, \\ \\ u_y^{n+1} - u_y^n = -\beta\frac{\delta t}{m}\left(\sqrt{(u_x^n)^2 + (u_y^n)^2}\right)u_y^n - g\delta t. \end{cases} \tag{24}$$

In these equations, u_x and u_y are the components of the velocity vector ($\mathbf{u}$), respectively, in x and y direction, and u^n stand for the velocity at time $n.\delta t$.

Knowing that the first time derivative of the position is the velocity, let say $u_x = \frac{dx}{dt}$ and $u_y = \frac{dy}{dt}$, the position of the disc at time $(n+1).\delta t$ can be deduced from equations (24) and position at previous time step by:

$$\begin{cases} x^{n+1} = -\beta\frac{\delta t^2}{m}\left(\sqrt{(u_x^n)^2 + (u_y^n)^2}\right)u_x^n + u_x^n\delta t + x^n, \\ \\ y^{n+1} = -\beta\frac{\delta t^2}{m}\left(\sqrt{(u_x^n)^2 + (u_y^n)^2}\right)u_y^n - g\delta t^2 + u_y^n\delta t + y^n. \end{cases} \tag{25}$$

As we can see, the theoretical trajectory can be calculated as long as the drag coefficient and its variation versus the velocity are known. For the present test

case on a smooth cylinder, for Reynolds number range previously mentioned, C_x varies linearly with the Reynolds number (see [19]). By linear interpolation of experimental data, we approximate the variation as:

$$C_x = 7.22 \times 10^{-5} Re_D + 0.927. \tag{26}$$

The simulation of this simple test-case is also performed by using `SPH-flow`, taking into account the fluid-structure interactions and viscous effects. The computational domain is a square with following extensions $[-0.4, 1.5]\times[-0.4, 1.5]\,\mathrm{m}^2$, the center of the disc being initially located at the origin of the framework $(x_0, y_0) = (0., 0.)$. Two different initial numbers of particles are used in this simulation: 1.0610^5 particles leading to an initial spatial discretization size $\delta x = 5.10^{-3}$ m, and 2.6610^6 particles corresponding to an initial $\delta x = 10^{-3}$ m.

In figure 5, we plot the solution of both analytical models (without drag force (21) and with drag force (25)) as well as the SPH solution. We first notice that differences appear rapidly between trajectories of analytical models, leading to a shorter throw range ($d_{scope} \simeq 0.95$) by taking into account drag force compared to the ballistic flight ($d_{scope} = u_0^2 sin2\alpha/g = 1$). Finally, SPH result compares well with the theoretical trajectory with the drag force, which was expected since the numerical model includes viscous effects.

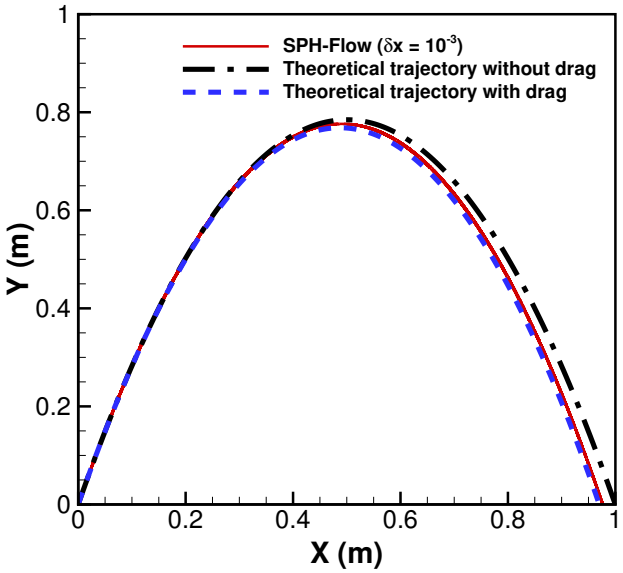

Fig. 5 Trajectory of a smooth cylinder shot at an initial velocity magnitude $u_0 = 4.118\,\mathrm{ms}^{-1}$ and an angle of 72.3° w.r.t. the horizontal axis: the SPH results are compared with the theoretical trajectory without drag (eq. 21) and the one with drag (eq. 25 and 26).

Forces applied to the solid body calculated by `SPH-flow` are compared on figure 6 with the theoretical drag force estimated from equations (22) and (26). Two parts on the force history can be distinguished on this figure: a part

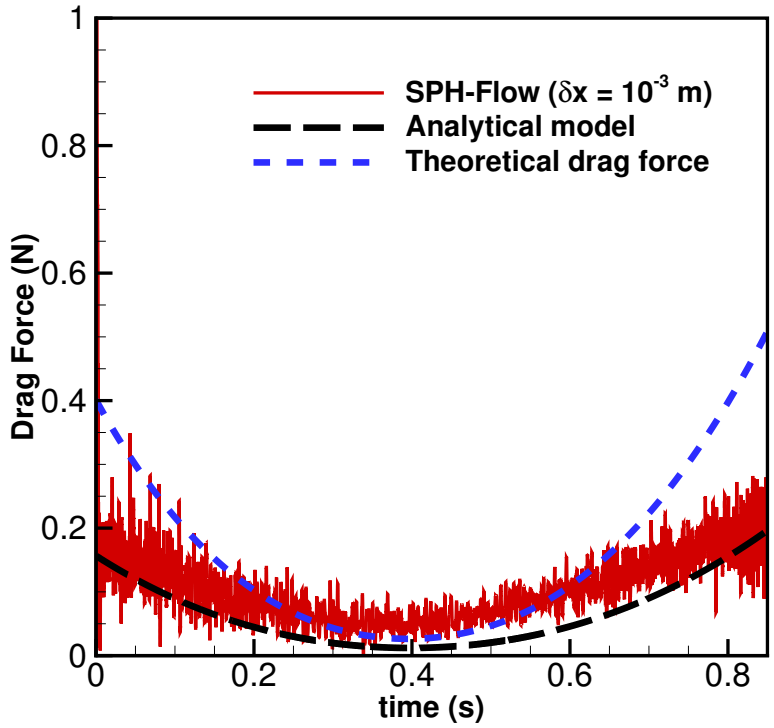

Fig. 6 Drag force applied onto the disc during the ballistic flight with an initial velocity magnitude 4.118 ms^{-1} with an angle of 72.3°: `SPH-flow` results (red bold line) are compared with the theoretical evolution (eq. 22 with eq. 26 and integration of eq. 24, blue dashed line) and an analytical model (eq. 22 with eq. 26 calculated with the velocity from the `SPH-flow`, black long-dashed line).

of decreasing forces which corresponds to the upward flight of the disc with a decreasing velocity, and a second part of increasing forces corresponding to the downward disc acceleration due to the gravity acceleration. Forces exerted onto the disc calculated by `SPH-flow` clearly exhibit large oscillations that can be attributed from one hand to the acoustic waves emitted by the disc displacement that interact with the solid body, and on the other hand by the turbulent regime of the flow in the vicinity of the disc that implies large unsteadinesses of the flow and therefore of the forces exerted on the body. At this Reynolds number range, the flow around the body does not stay symmetric

and lift forces, while weak compared to the drag force, are then created that affect the drag forces. We can easily see that oscillation magnitudes are large when velocity magnitudes are important, let say at the beginning of the flight and during the downward motion when the disc accelerates. On the opposite oscillations are damped around the apogee of the disc when the velocity is the lowest. This is fully in agreement with the role of the acoustic waves and the turbulent regime.

Although the variation of the drag force calculated from the flow solver has a similar trend as the theoretical force history, the simulated forces do not overlap the theoretical values (from eq. 22 with eq. 26). In fact, values taken as reference do not exactly mimic reality since forces exerted on the body is only restricted to the theoretical drag force in the equation derivation (24, 25) that has been approximated, mainly by estimated the values of the drag coefficient versus the theoretical velocity values (eq. 24). A better agreement is recovered if we compare the drag force from the `SPH-flow` simulation with the approximated drag force from equations (22) and (26), however calculated with the instantaneous velocity and Reynolds number recorded from the `SPH-flow` simulation (see fig. 6).

These remarks explain why, following the theoretical approach, it is difficult to accurately predict a ballistic flight when unsteady aerodynamic loads are at play. Therefore, to account for these aerodynamic effects, a flow solver is necessary. In this case, the `SPH-flow` solver gives results that mimic right well the real flight of a disc in air. It is with confidence that we could undertake simulations of the flight of a badminton shuttlecock.

5 Numerical results of the flight of the proposed model of a badminton shuttlecock.

Following validations with `SPH-flow`, we now investigate the simulation of the flow in the vicinity of the proposed model of a badminton shuttlecock.

5.1 Simulation of a shuttlecock in wind tunnel.

As it is often done in scientific works devoted to study the flow around a badminton shuttlecock, we would like first to determine the drag coefficient (C_x) of our proposed model of the shuttlecock with respect to the Reynolds number. We consider the proposed 2D model of the shuttlecock kept fixed in the middle of an aerodynamic wind tunnel with a constant air mass flow rate. The computational domain is limited at the bottom and the top by two parallel walls bounding the wind tunnel, on which no-slip boundary conditions are applied. At the inlet of the computational domain a constant mass flow rate is prescribed defining the constant velocity magnitude u_0. Several flow velocities has been prescribed ($2.6\,\mathrm{ms}^{-1} \leq u_0 < 70\,\mathrm{ms}^{-1}$) representing usual velocity range of the shuttlecock during a game. The corresponding Reynolds numbers,

based on the diameter of the skirt (D), are in-between $10^4 \leq Re_D \leq 2.6 \times 10^5$. The inlet pressure is defined so that it is of the order of the dynamic pressure $P = \rho u^2/2$.

The computational domain extents are: $(x, y) \in [0., 0.8] \times [-0.175, +0.175]$ m^2. Simulations were performed by using a spatial discretization of $\delta x = 5 \times 10^{-4}$ m (checked as spatially converged) corresponding to about 1.12×10^6 initial number of particles. The simulation was run over 1 second.

As the shuttlecock is assumed to remain fixed, the effect of gravity is not taken into account and the only force exerted on the shuttlecock is the drag force that is calculated by `SPH-flow`. On figure 7, we plot the magnitude of the

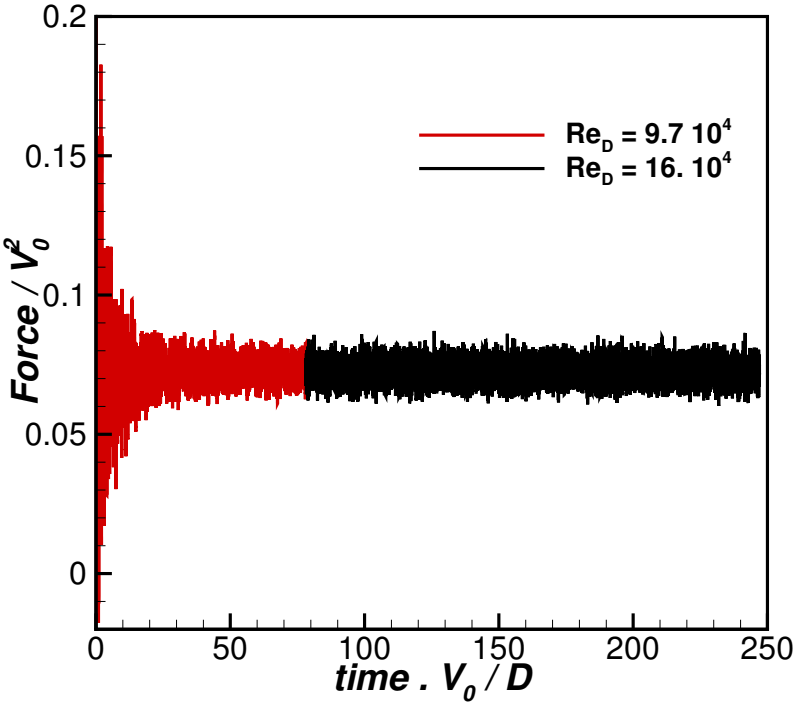

Fig. 7 History of the resultant of forces exerted on the shuttlecock fixed in a wind tunnel for two Reynolds numbers: $Re = 9.7 \times 10^4$ ($V_0 = 26$ ms^{-1}) and $Re = 16 \times 10^4$ ($V_0 = 42.92$ ms^{-1})

drag force, calculated from the solver, dimensionless by the square of the velocity, versus the dimensionless time for two Reynolds number. After a transient period for initiating the flow around the shuttlecock, the drag force oscillates around a stable average value meaning that the flow is fully developed and the numerical solution reaches a statistically converged state. These high fre-

quency oscillations come from both the acoustic waves and the unsteadinesses linked to the turbulent regime of the flow. The oscillation magnitudes of the dimensionless drag force as well as its mean value seem almost independent of the Reynolds number, which means that the C_x coefficients will not vary very much with respect to the Reynolds number. From the time averaged value of the drag force (F_{drag}), calculated from data recorded in the last part of the simulation, the drag coefficient (C_x) is then deduced from equation (22). We recall that the spanwise length $H = 1$ m (because of 2D model) and $D = 0.066$ m the diameter of the skirt (see table 1). Then, the drag coefficient (C_x) are plotted in figure 8 versus the Reynolds number in the range previously mentioned. Results show that the drag coefficient varies very little as a function of the Reynolds number in the range of the velocity flow simulated. The average value of C_x is around 1.82.

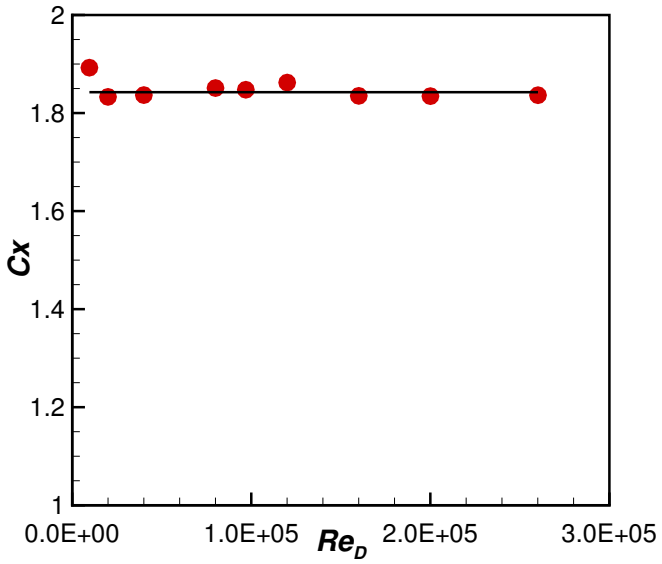

Fig. 8 Variation of the drag coefficient Cx as a function of the Reynolds number of a shuttlecock kept fixed in wind tunnel.

It is interesting to compare this numerical value of C_x to the experimental one recorded by C. Cohen *et al.* [4] with a feather shuttlecock fixed in a wind tunnel, who recorded an almost constant C_x values versus the Reynolds number (in the range studied), with a mean value of $C_x = 0.65 \pm 0.005$ [4]. The difference between the numerical ($C_x = 1.82$) and the experimental ($C_x = 0.65$) values, though significant, can be explained by the 2D/3D effect since, in this Reynolds number range, the drag coefficient of a smooth cylinder is three times larger than the one of a smooth sphere, for the same diameter (see [19]). It is

then quite reasonable to think that the present numerical results obtained in the 2D framework with the proposed modeled shuttlecock is in a quite good agreement with the C_x averaged value experimentally recorded in 3D for a feather shuttlecock [4].

Simulations give easily access to instantaneous velocity components and static pressure field, mainly within the skirt which is difficult to experimentally probe. In figure 9, snapshots of the longitudinal (u_x/u_0) and the vertical (u_y/u_0) components of the velocity, dimensionless by the infinite velocity (u_0), are shown in the vicinity of the shuttlecock for a statistically converged state obtained at a dimensionless time $t = 227$ for an infinite velocity $u_0 = 42.92$ ms^{-1}(corresponding to a Reynolds number $Re_D = 16 \times 10^4$). The corresponding instantaneous dimensionless velocity magnitude, and the static pressure dimensionless by the dynamic pressure, are also given in figure 10. Only instantaneous fields can be analyzed in the SPH method framework because particles carrying the flow information move along time and are rarely located at the same place for several time steps, forbidding correct time averaging of a quantity.

At the stagnation point located at the upstream point of the cork, the flow is at rest and consequently the pressure reaches its maximum value (fig. 10). An important acceleration of the flow of about 30 % takes place from side to side of the shuttlecock (fig. 10-left). A wide area of velocity deficit takes place within the skirt with a recirculation bubble just downstream the backward face of the cork (negative longitudinal velocity Fig. 9-left). The recirculation bubble ends up when the flow feeding from the external flow inside the skirt is made possible through the holes in the skirt. Negative values at the top part and positive values at the bottom part of the skirt are clearly visible on the vertical component of the velocity (u_y) (Fig. 9), participating in the feeding mechanism that weakens the velocity deficit. This region of velocity deficit also extends in the wake of the shuttlecock, contributing then to its drag. The corresponding pressure field exhibits the top/bottom non symmetry of the flow with low pressure regions when the flow locally accelerates, mainly in region where feeding flow inside the skirt occurs, where local vortices are created contributing to unsteady constraints on the shuttlecock. Just downstream the skirt, we can easily see the shear layer originating from the end of the skirt at the confluence of inside and outside flows, that also contribute to the drag.

5.2 Simulations of the badminton shuttlecock trajectory.

In the previous section, the shuttlecock was fixed and was not subjected to the force of gravity. We are now going to simulate the flight of a free shuttlecock that will be shot with different velocities and departure angles. Simulations using `SPH-flow` were undertaken with the proposed model of the 2D shuttlecock (Fig. 3) with characteristics that was previously presented (see table 1). The shuttlecock is initially located at the origin $(x_0, y_0) = (0., 0.)$ of the framework (Fig. 11). The computational domain is defined as $(x \times y) \in$

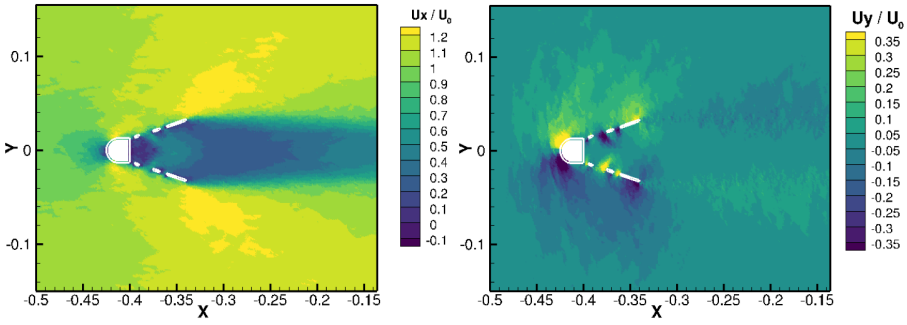

Fig. 9 Snapshots at a dimensionless time $t = 227$ of the instantaneous velocity field of the flow in the vicinity of the shuttlecock fixed in a wind tunnel obtained with `SPH-flow` for an infinite velocity $u_0 = 42.92$ ms^{-1}for the finest spatial resolution ($\delta x = 5 \times 10^{-4}$ m): on the left, the longitudinal component (u_x/u_0), and on the right, the vertical component (u_y/u_0).

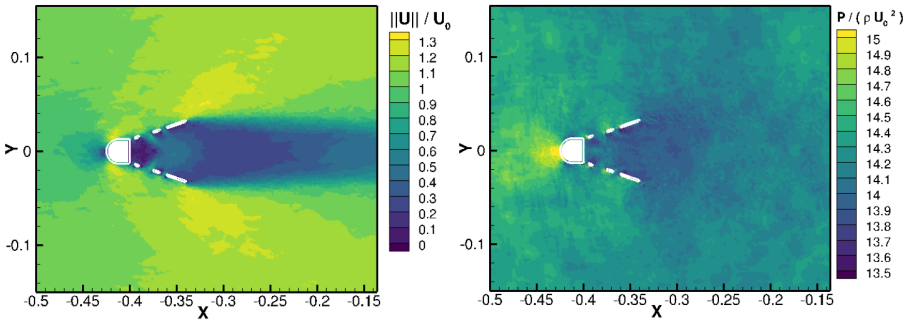

Fig. 10 Instantenous dimensionless velocity magnitude ($||u||/u_0$), and the instantaneous pressure (P) field, dimensionless by the infinite dynamic pressure (ρu_0^2) at a dimensionless time $t = 227$ around the shuttlecock fixed in a wind tunnel obtained with `SPH-flow` for an infinite velocity $u_0 = 42.92$ ms^{-1}on the finest spatial resolution ($\delta x = 5 \times 10^{-4}$ m).

$[-0.2, 11.] \times [-0.2, 4.]\,\mathrm{m}^2$. The initial spatial resolution is $\delta x = 4 \times 10^{-3}$ m (leading to about 3×10^6 particles).

The fluid has following properties: dynamic viscosity $\mu = 1.7 \times 10^{-5}$ Pa s and density $\rho = 1.2\,\mathrm{kg\,m}^{-3}$. The acceleration of gravity g is equal to $9.81\,\mathrm{m\,s}^{-2}$.

Several configurations with different initial velocities (u_0) and departure angles (ψ, defined as in Fig. 11) have been simulated, and are reported in table (2). They are inspired by the work undertaken by Cohen *et al.* [4], on the flight of a feather shuttlecock.

Trajectories obtained from `SPH-flow` are shown in figure 12 for different initial sets of departure velocities and angles. It is clear that trajectories are far away from the parabolic trajectory meaning that the drag force, at least,

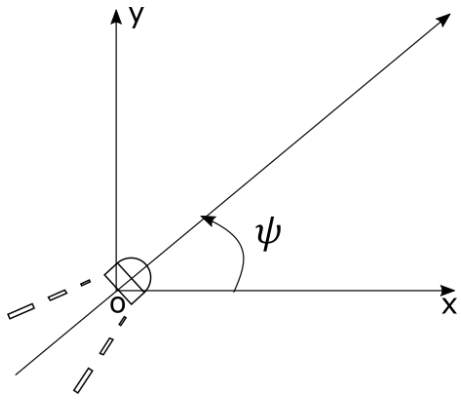

Fig. 11 Initial location of the shuttlecock and definition of the angle ψ with respect to the horizontal axis (Ox).

u_0 [ms^{-1}]	ψ [°]	u_0/u_{term}
6.8	55.	1.23
10.	45.	1.71
13.4	58.	2.45
19.8	39.	3.58
24.7	44.	4.46
37.6	38.	6.79

Table 2 Initial parameters for shuttlecock trajectory: velocity magnitude u_0 and departure angle ψ.

plays an important role on the shuttlecock flight. These trajectories mostly follow what is called the Nicollo Tartaglia's trajectory [20]: the shuttlecock follows first a straight line, followed by an apogee flight with asymmetry at the top and finally a vertical drop. To explain this type of trajectory, we come back to the equation (23) of a solid body mouvement subjected to its weight and the drag forces. If we look at which velocity the weight is compensated by the drag of the body, we obtain what we call the *terminal velocity* that cancels the body acceleration ($\frac{d\mathbf{u}}{dt} = 0$), defined as:

$$u_{term} = \sqrt{\frac{2.Mg}{\rho S C_x}} \tag{27}$$

Using this terminal velocity into equation (23), this equation can be re-casted in:

$$\mathbf{g} - \frac{g}{u_{term}^2} u\mathbf{u} = \frac{d\mathbf{u}}{dt} \tag{28}$$

We can qualitatively analyze equation (28):

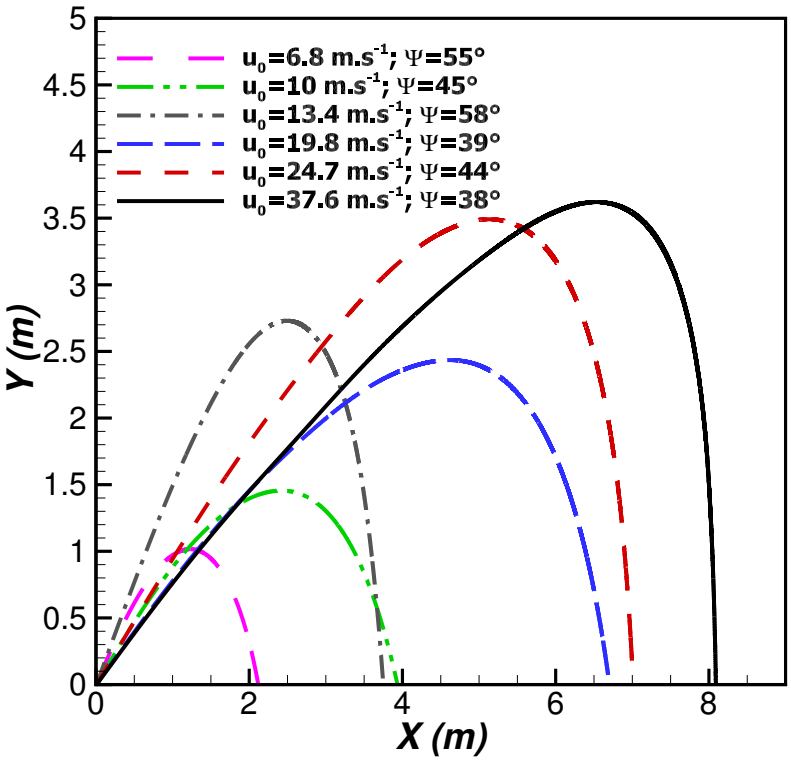

Fig. 12 Trajectories of the 2D model of the badminton shuttlecock calculated by using `SPH-flow` with different departure velocities and angles.

- if initially $u \ll u_{term}$ (*i.e.* $g \gg \frac{g}{u_{term}^2}u^2$): the drag forces are negligible and the trajectory is parabolic as defined by the equation (21) taking only in account the body weight;
- if initially $u \gg u_{term}$ (*i.e.* $g \ll \frac{g}{u_{term}^2}u^2$): the equation of motion is reduced to $-\frac{g}{u_{term}^2}u\mathbf{u} = \frac{d\mathbf{u}}{dt}$ that gives a rectilinear trajectory oriented in the shooting angle direction.

We also define the ratio $\mathcal{L} = u_{term}^2/g$ as the *aerodynamic length* representing the typical vertical drop length required for a body to reach its terminal velocity. At the beginning of the flight, drag acting, the shuttlecock will lose energy and thus decelerates over this aerodynamic length $\mathcal{L}$ (Fig. 12). Deceleration goes on until the shuttlecock reaches a situation where both the gravity and the drag forces cannot be neglected. This stage corresponds to the asymmetric zone at the apogee of the flight (Fig. 12). The equilibrium state is then reached when the velocity of the shuttlecock is close to its terminal velocity. Shuttlecock acceleration being cancelled, it falls almost vertically like

in a free fall. This explains the Nicollo Tartaglia type trajectory followed by the badminton shuttlecock when the initial velocity is much greater than the terminal velocity.

This behaviour is clearly reproduced by simulations for extreme configurations. We calculated the terminal velocity (u_{term}) for present configurations, assuming that the drag coefficient (C_x) is constant and independent of the Reynolds number, and equal to the value found in the previous simulation (*i.e.* $C_x = 1.82$). We then report the ratio of the departure velocity with this terminal velocity (u_0/u_{term}) in the last column of table 2. For instance $u_0 = 37.6\,\mathrm{ms}^{-1}$, we get $u_0 \gg u_{term}$ and the rectilinear departure is obtained by neglecting the effect of gravity as well as, at last times of the flight, the almost vertical fall due to the importance of gravity. On the opposite, considering a low initial speed, for instance $u_0 = 6.8\,\mathrm{ms}^{-1}$ corresponding to $u_0 \simeq u_{term}$, the trajectory of the shuttlecock is almost parabolic (Fig. 12). Among projectiles in sports, badminton is the only one that can have a very high ratio u_0/u_{term}, explaining these wide range of trajectories.

Although simulations are conducted in a 2D framework with important assumption on shuttlecock geometry, `SPH-flow` produces numerical trajectories that mimic very well real trajectories since they are similar to trajectories that have been studied in the work of Cohen *et al.* [4].

5.3 Simulations of the shuttlecock movements during a flight.

The previous section looked at the flight of a badminton shuttlecock when the cork is turned forward. However, the shuttlecock is normally hit by the racket on the cork that is turned backward with respect to the initial velocity. In the first stage of its flight, the badminton shuttlecock presents an atypical flight since it starts by turning over to position itself with the cork towards the front of its trajectory. In this section, we would like to investigate by numerical simulations the different sequences of the badminton shuttlecock movement during its flight after being hit by the racket.

Simulations are conducted by using the same parameters as the ones defined in the previous section. The shuttlecock is however initially positioned with a departure angle $\psi = -175°$ (Fig. 11). We suppose that when the racket hits the cork, the initial velocity of the center of mass of the shuttlecock is $u_0 = 18.5\,\mathrm{ms}^{-1}$.

During the simulation, snapshots of the velocity field are recorded every $\times 10^{-2}$ second, and a chronophotography of the shuttlecock positions every two frames is shown in figure 14. As the cork of the shuttlecock is heavier than its skirt, the shuttlecock in a first stage turns over by inertia so that the cork always stays in the lead. Despite this reversal movement, the shuttlecock never completes a full turn. It turns in one direction with a variation of the angle less than 360° and then changes direction of rotation. The variation of the angle (ψ w.r.t. the horizontal axis (O, x)) during the flight is reported in figure 15.

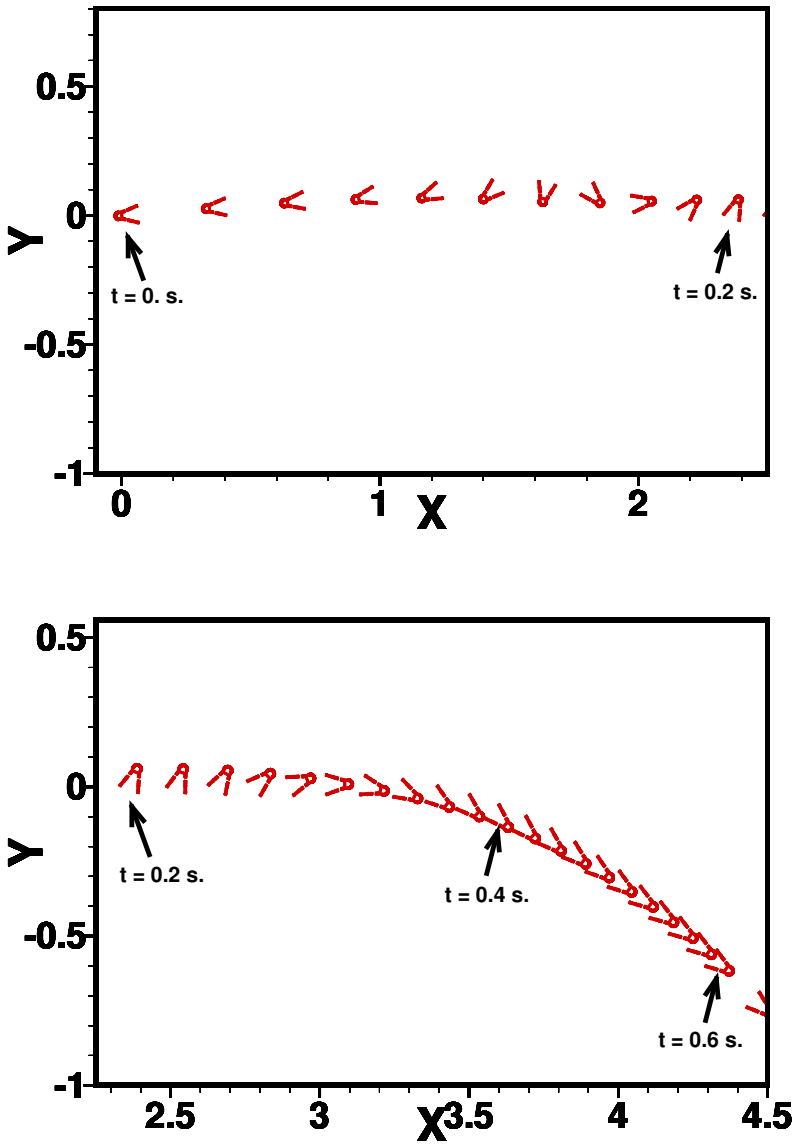

Fig. 13 Chronophotography of the 2D shuttlecock model with an initial velocity $u_0 = 18.5\,\mathrm{ms}^{-1}$ and an initial departure angle $\psi_0 = -175°$: the start of the turning over phase, at the top, and, at the bottom, the end of the turning over phase followed by the start of the oscillation phase (at the bottom). Time interval between two successive images is $2. \times 10^{-2}$ second.

The first stage of the movement is the turnaround phase that lasts about 0.4 second (Fig. 15) where the angle of the shuttlecock (ψ) increases rapidly

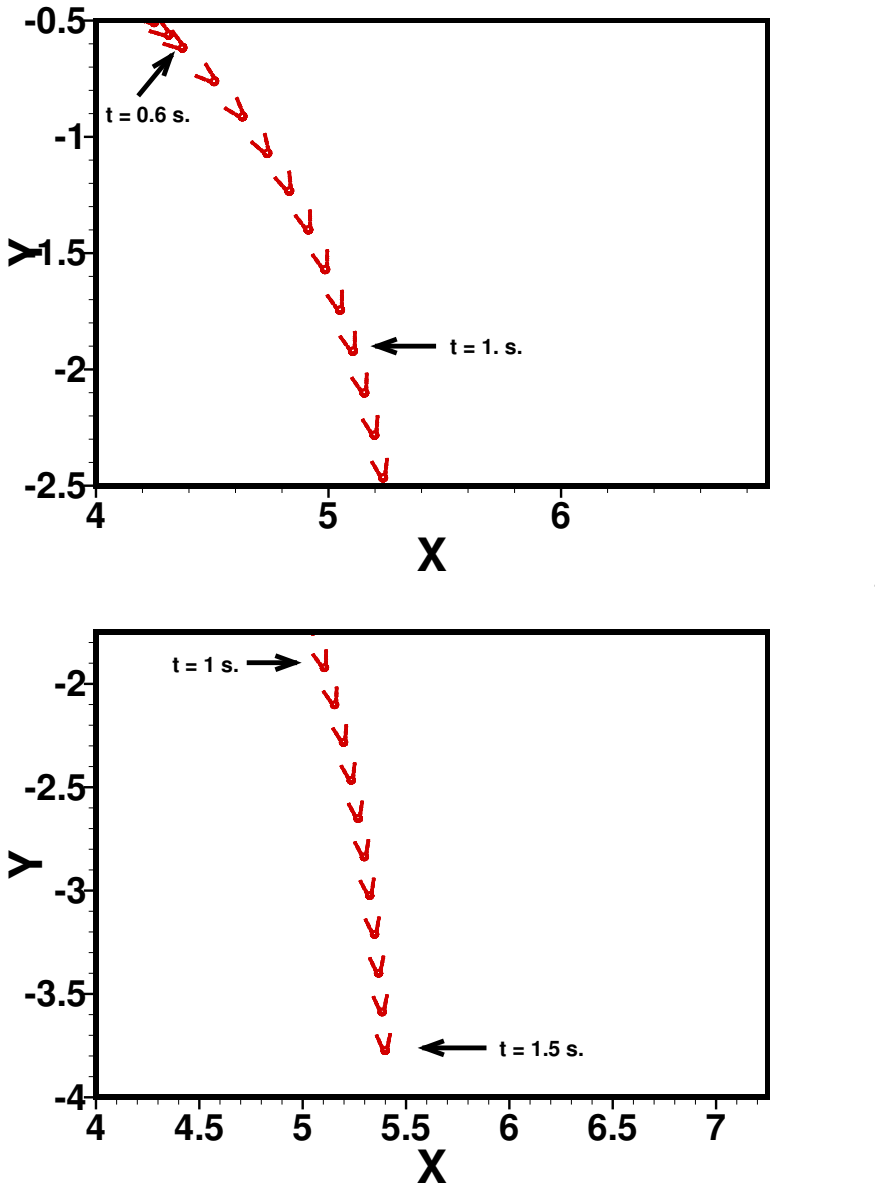

Fig. 14 Chronophotography of the 2D shuttlecock model with an initial velocity $u_0 = 18.5\,\mathrm{ms}^{-1}$ and an initial departure angle $\psi_0 = -175°$: The oscillation phase, at the top, followed by the stabilization phase, at the bottom. Time interval between two successive images is $5. \times 10^{-2}$ second.

to become positive (up to $\psi = 70°$) and then decreases so that the shuttlecock is positioned with the cork down (negative ψ values). This first stage is mainly

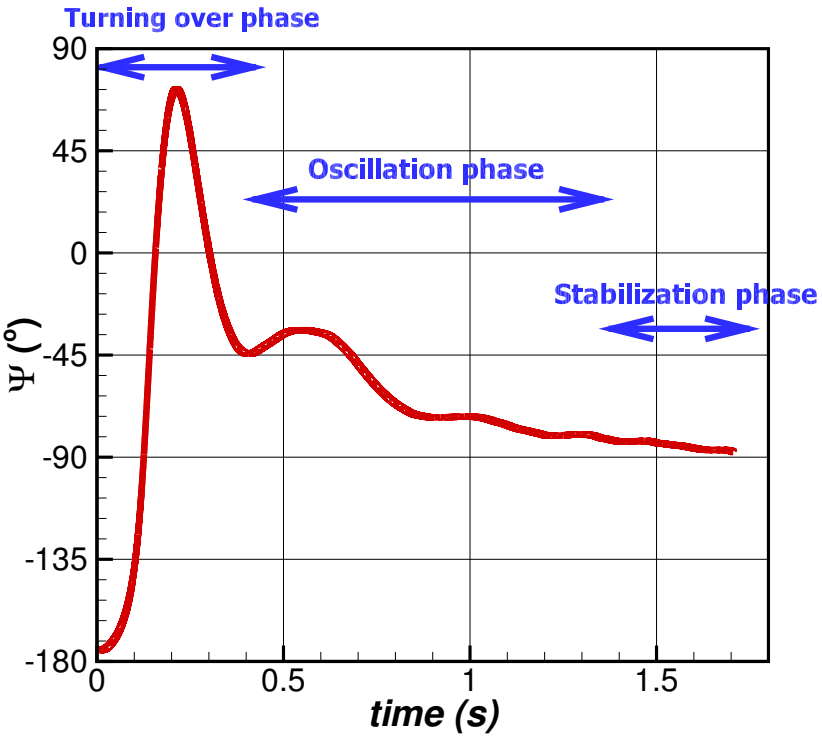

Fig. 15 Variation of the angle ψ during the flight: the initial angle is $\psi = -175°$.

due to inertia effect because of the heavier weight of the cork than the skirt. Then, in a second stage, the shuttlecock oscillates around a mean trajectory for about one more second before stabilizing in the last stage. Oscillations are attributed to a competition between the inertia effect and the unsteady forces exerted on the shuttlecock mainly due to the unsteady wake with street of alternate vorticies. As the friction drag is at play, oscillation amplitudes and frequencies are damped progressively until the shuttlecock recovers a stable and rectilinear motion. We say that the shuttlecock recovers a stable flight when its central axis is collinear with its velocity vector. This is attained during its free fall when $\psi = -90°$.

These three stages highlighted in this simulation are very comparable to what has been experimentally visualized and analyzed by Cohen *et al.* [4]. To our knowledge, it is the first time that the special movement of a badminton shuttlecock during its flight is simulated with large displacements. This was made possible thanks to the computation with the SPH approach that takes into account the physical and geometrical properties of a badminton shuttlecock as well as the fluid/structure interaction that accounts for dynamic forces exerted on the shuttlecock during its flight.

6 Conclusion and prospect.

In this paper, we investigated the capability of a numerical meshless method, the SPH method, to predict the whole flight of a badminton shuttlecock just after the racket hit the cock stopper. As a first step, we restricted our study to the 2D framework, and we proposed a 2D shuttlecock model with same characteristic dimensions and weights as a real shuttlecock. The numerical method is first presented with the application of the SPH method to the numerical treatment of the weakly compressible Navier-Stokes equations, the equations of the solid motion subjected to external forces, and the coupling procedure in the fluid-solid interaction.

We first validated the numerical approach on a simple test-case of a ballistic flight of a cylinder. The theoretical cylinder trajectory taking into account the aerodynamic forces is well recovered by the simulation. The drag force calculated along the SPH simulation is in a good agreement with the theoretical drag force estimated with a prescribed C_x law using the instantaneous velocity recorded from the SPH simulation.

Once the flow solver validated, we investigated flights of the proposed 2D shuttlecock model. Similarly to previous numerical studies [10,11], we simulated the air flow around a shuttlecock fixed in a wind tunnel. The variation versus the Reynolds number of the drag coefficient (C_x) is shown to be in a quite good agreement with averaged experimental values from the literature. We also investigated the badminton shuttlecock trajectory in the most stable configuration where the cock stopper is already in front of the trajectory. Although 2D, we showed that trajectories are similar to the ones studied in the work of Cohen *et al.* [4] for feather shuttlecock. We finally simulated the complete flight of the badminton shuttlecock, from the departure with the cock stopper oriented backward, to the final stage of the flight with a stable trajectory. Main characteristics of the flight as well as the shuttlecock behavior during the flight are reproduced thanks to the numerical approach. We analyzed all the phases of the flight and showed that there are three stages during the flight. At the early stages, there exists a turning over phase that does not last long, due to the inertia effect because the weight of the cork is much heavier than the skirt. This phase is followed by an oscillation phase, lasting longer, that is attributed to a competition between the inertia effect and the unsteady aerodynamic forces exerted on the shuttlecock. As energy is dissipated, oscillation amplitudes are progressively damped, in a third phase, until the shuttlecock recovers a stable and rectilinear motion. These three stages highlighted in these simulations are very comparable to what has been experimentally visualized and analyzed by Cohen *et al.* [4]. To our knowledge, it is the first time that the complete flight of a badminton shuttlecock with displacements over a large extent, has been numerically simulated with good predictions of the special movements of the shuttlecock during its flight. This was made possible thanks to the computation with the SPH approach that takes into account the physical and geometrical properties of the badminton

shuttlecock as well as the fluid/structure interaction that accounts for dynamic forces exerted on the shuttlecock during its flight.

In this study, we only investigated mouvements of the badminton shuttlecock when it was hit without an initial angular momentum. However, it is the action of the racket on the badminton shuttlecock that largely determines the variety of the shuttlecock flights. The shuttlecock thus follows a variety of trajectories depending on the type of stroke the experienced player do (spin-in, spin-out, increasing the initial spin, ...). In the future, we would like to get closer to reality by simulating badminton shuttlecock flights by taking into account the initial effects given to the shuttlecock during the strike. This is made possible since the numerical methods used in this study are also valid in 3D.

Acknowledgment

Simulation results presented in this article were obtained with `SPH-flow`, courtesy of Nextflow Software. `SPH-flow` is co-developed with Ecole Centrale de Nantes research departments. To get more information about Nextflow Software company and products, go to www.nextflow-software.com or send an e-mail to contact@nextflow-software.com. The present work was performed on computing resources provided by CRIANN (Normandy, France). Authors greatly thank this computing center.

A Appendices

A.1 Center of mass of the shuttlecock

The movement of a rigid body is defined with respect to its center of mass (eq. 19) that needs to be accurately calculated. By definition, the position $\mathbf{r_G}(x_G, y_G, z_G)$ of center of mass G is the point located at the mean position of the mass of the body. For a homogeneous body with a simple geometry, the center of mass is generally the geometric center of the object. However, in the present case, the shuttlecock has a complex geometry and is inhomogeneous (cork and skirt do not have the same density). Finding its center of mass therefore amounts to define the barycenter of our model. The barycenter is the equilibrium point of different weighted points in a system. Since the shuttlecock has a symmetry with respect to its central axis (Ox) (see fig. 3), its center of mass must then be located on this axis (Ox axis). By definition, the x coordinate of the center of mass location of a body is obtained by:

$$x_G = \frac{\int_{\mathcal{V}} \rho(m) x d\mathcal{V}}{m}, \tag{29}$$

where $\mathcal{V}$ is the volume of the body, $\rho(m)$ its density, and m its mass defined as $m = \int_{\mathcal{V}} \rho(m) d\mathcal{V}$.

The barycenter of the system, made up of the three parts, is calculated from:

$$\overrightarrow{OG} = \frac{m_1 \overrightarrow{OG_1} + m_2 \overrightarrow{OG_2} + m_3 \overrightarrow{OG_3}}{M} \tag{30}$$

where O is the origin of the frame, set on the backward face of the cork (see fig. 3), G_1, G_2, and G_3 are centers of gravity of, respectively, the half disc, the rectangular part of the cork

and the skirt, M is the mass of the entire shuttlecock, and m_1, m_2, and m_3 are the mass of aforementioned parts.

- $\overrightarrow{OG_1}$ is easily calculated because it is the center of mass of a half-disc which is x_{G1}=$4R\pi/3$ w.r.t. the disc center. With respect to the present frame (see figure 3), $\overline{OG_1} = -(h - d/2 + x_{G1}) = -17.402\,\text{mm}$;
- $\overrightarrow{OG_2}$ is also easy to calculate since it is the center of mass of a rectangle which is $x_{G2} = (h - d/2)/2$ w.r.t. the rectangle center. With respect to the present frame (see figure 3), $\overline{OG_2} = -(h - d/2)/2 = -5.9\,\text{mm}$;
- $\overrightarrow{OG_3}$ is a little bit more complex to calculate because of the skirt geometry. Using the definition (29) applied to the skirt, the abscissa location of the center of mass is obtained by:

$$x_{G3} = \frac{\int_S x dS}{S},$$

where $S = dL + (D - d)L/2 = (D + d)L/2$ is the surface of the skirt. As we can see on figure 3, the skirt is formed by trapezes which are limited on the upper and lower surfaces by two lines of equations:

$$f_1(x) = \frac{\frac{D}{2} - \frac{d}{2}}{L}x + \frac{d}{2}$$

and

$$f_2(x) = \frac{-\frac{D}{2} + \frac{d}{2}}{L}x - \frac{d}{2}$$

Following the definition given by equation (29), the abscissa of the barycentre of the skirt is then:

$$x_{G3} = \frac{\displaystyle\int_0^L x \left(\int_{f_1(x)}^{f_2(x)} dy \right) dx}{S} = \frac{2L(D + \frac{d}{2})}{3(d + D)}. \tag{31}$$

With respect to the present frame (see figure 3), $\overline{OG_3} = 34.285\,\text{mm}$.

Having defined abscissae of the centers of mass of each part of the shuttlecock model, we can calculate the coordinate of the center of mass of the shuttlecock with equation (30). With respect to the present frame (see figure 3), the location of the center of mass of the shuttlecock is:

$$\overline{OG} = 7.28\,\text{mm}.$$

The location of the center of mass (point G) is identified on figure 3, in the frame of the shuttlecock.

A.2 Inertia matrix of the shuttlecock

The inertia matrix quantifies the resistance of a body subjected to a rotation (see eq. 20). For the badminton shuttlecock flight, it is one of the important elements to mimic the movement of the shuttlecock. By definition, the inertia matrix of a solid body (S) with respect to its center of mass G can be expressed as:

$$I_G = \begin{pmatrix} A & -F & -E \\ -F & B & -D \\ -E & -D & C \end{pmatrix} = \begin{pmatrix} \int_{\mathcal{V}}(y^2 + z^2)dm & -\int_{\mathcal{V}} xydm & -\int_{\mathcal{V}} xzdm \\ -\int_{\mathcal{V}} xydm & \int_{\mathcal{V}}(z^2 + x^2)dm & -\int_{\mathcal{V}} yzdm \\ -\int_{\mathcal{V}} xzdm & -\int_{\mathcal{V}} yzdm & \int_{\mathcal{V}}(x^2 + y^2)dm, \end{pmatrix} \tag{32}$$

where $dm = \rho d\mathcal{V}$, $\mathcal{V}$ is the volume of the solid (S), and (x, y, z) are coordinates of each point of this solid expressed in the frame that has the center of mass as origin (G,$\mathbf{x}$,$\mathbf{y}$,$\mathbf{z}$).

As the shuttlecock model is an assembly of several solid parts (half disc for forward part of the cork, a rectangle for the backward part of the cork, and trapezes for the skirt), the moment of inertia with respect to a point of the whole shuttlecock (let say the center of mass

G) can be calculated as the sum of moments of inertia of each solid part with respect to the same point. However, the center of mass $G(x_G, y_G, z_G)$ of the shuttlecock does not coincide with the centers of mass of each solid $G_n(x_{G_n}, y_{G_n}, z_{G_n})$ such that n corresponds to the number of solid parts comprising the shuttlecock (in fact, $n = 3$). Applying the Huyguens' theorem, the moment of inertia w.r.t. the center of mass (G) of the shuttlecock of each solid part is:

$$I_{G_n} = I_n + m_n \underline{\underline{d}}, \tag{33}$$

where I_{G_n} denotes the inertia matrix of the solid part n with respect to the center of mass G of the whole shuttlecock, I_n is the inertia matrix of the solid part n relative to its center of mass G_n, and m_n the mass of the solid part n. $\underline{\underline{d}}$ is a distance matrix expressed as:

$$\underline{\underline{d}} = \begin{pmatrix} (b^2+c^2) & -ab & -ac \\ -ab & (c^2+a^2) & -bc \\ -ac & -bc & (a^2+b^2), \end{pmatrix}$$

where a, b, c are the components of $\overrightarrow{GG_n}$, the vector which separates the center of mass G_n of each solid part from the center of mass G of the whole shuttlecock. Finally, we could calculate the inertia matrix (I_G) of the whole shuttlecock with respect to its center of mass G by:

$$I_G = \sum_{k=1}^{n} I_{G_k}.$$

As we propose a 2D shuttlecock model, we could apply a symmetry with respect to the x-axis, and we get $E = F = D = 0$ in the equation (32). By applying the previous equations to the proposed 2D model of the shuttlecock, we obtain the following inertia matrix (expressed in $\mathrm{kg\,m^2}$):

$$I_G = M. \begin{pmatrix} 3.4153\,10^{-4} & 0 & 0 \\ 0 & 3.6881\,10^{-4} & 0 \\ 0 & 0 & 7.1034\,10^{-4} \end{pmatrix} \tag{34}$$

with M the total mass of the shuttlecock (expressed in kg). This inertia matrix was employed throughout our simulations presented in the following sections.

References

1. Cooke, A. J. Shuttlecock aerodynamics. *Sports Eng.*, **2**: 85–96, 1999.
2. Alam, F.; Chowdhury, H.; Theppadungporn, C. and Subic, A. Measurements of aerodynamic properties of badminton shuttlecocks. *Procedia Eng.*, **2**: 2487–2492, 2010.
3. Julien Le Personnic, Firoz Alam, Laurent Le Gendre, Harun Chowdhury, Aleksandar Subic, Flight trajectory simulation of badminton shuttlecocks, *Procedia Engineering*, **13**: 344–349, 2011.
4. Cohen, C.; Darbois Texier, B.; Quéré, D. and Clanet, C. The physics of badminton, *New Journal of Physics*, **17**, 063001, 2015
5. Shah, K.; Shakya, R. and Mittal S. Aerodynamic forces on projectiles used in various sports. *Phys. Fluids*, **31**: 015106, 2019.
6. Cooke, A. J. Computer simulation of shuttlecock trajectories. *Sports Eng.*, **5** 93–105, 2002.
7. Chen, L. M.; Pan, Y. H. and Chen, Y. J. A study of shuttlecock?s trajectory in badminton. *Journal of Sports Science and Medicine*, **8**: 657–662, 2009.
8. Nakagawa, K.; Hasegawa, H.; Murakami, M. and Obayashi, S. Aerodynamic Properties and Flow Behavior for a Badminton Shuttlecock with Spin at High Reynolds Numbers, *Procedia Engineering* **34**: 104–109, 2012.
9. Seigo Kitta, Hiroaki Hasegawa, Masahide Murakami, Higeru Obayashi Aerodynamic properties of a shuttlecock with spin at high Reynolds number *Procedia Engineering*, **13**: 271–277, 2011.

10. Verma, A.; Desai, A.; Mittal, S. Aerodynamics of badminton shuttlecocks, *Journal of Fluids and Structures*, **41**: 89–98, 2013
11. Hart, J. Simulation and understanding of the aerodynamic characteristics of a badminton shuttle, *Procedia Engineering*, **72**: 768–773, 2014.
12. Donea, J.; Giuliani, S. and Halleux, JP. An arbitrary Lagrangian-Eulerian finite element method for transient dynamic fluid-structure interactions. *Computer Methods in Applied Mechanics and Engineering*, **33**(1): 689–723, 1982.
13. Le Tallec, P. and Mouro, J. Fluid structure interaction with large structural displacements. *Computer Methods in Applied Mechanics and Engineering*, **190**(24): 3039–3067, 2001.
14. Fadlun, E. A.; Verzicco, R.; Orlandi, P. and Mohd-Yusof, J. Combined immersed-boundary finite-difference methods for three-dimensional complex flow simulations. *Journal of Computational Physics*, **161**(1): 35–60, 2000.
15. Tseng, Y. H. and Ferziger, J. H. A ghost-cell immersed boundary method for flow in complex geometry. *Journal of Computational Physics*, **192**(2): 593–623, 2003.
16. Monaghan, J. J. An introduction to SPH. *Computer Physics Communications*, **48**: 88–96, 1988.
17. Bate, M. R.; Bonnell, I. A. and Price, N. M. Modelling Accretion in Protobinary Systems. *Mon. Not. R. Astron. Soc.*, **277**: 362–376, 1995.
18. Maurel, B. Modélisation par la méthode SPH de l'impact d'un réservoir rempli de fluide. *Thse de doctorat*, INSA Lyon, 2008
19. Hochstein, J. I. Munson, Young and Okiishi's Fundamentals of Fluid Mechanics, 8th edition, John Wiley & Sons Eds, 2015.
20. Darbois Texier, B.; Cohen C.; Dupeux, G., Qur, D. and Clanet, C. On the size of sports fields. *New Journal of Physics*, **16**: 033039, 2014.
21. Monaghan, Joseph J. Simulating free surface flows with SPH. *Journal of Computational Physics*, **110**(2): 399–406, 1994.
22. Libersky, Larry D.; Petschek, Albert G.; Allahdadi, Firooz A. High Strain Lagrangian Hydrodynamics. *Journal of Computational Physics*, **109**: 67–75, 1993.
23. Randles, P. W.; Libersky, L. D. Smoothed Particle Hydrodynamics: Some recent improvements and applications. *Computer Methods in Applied Mechanics and Engineering*, **139**: 375–408, 1996.
24. Antoci, C. ; Gallati, M. ; Sibilla, S. Numerical simulation of fluidstructure interaction by SPH. *Computers & Structures*, **85**11: 879–890, 2007.
25. Colagrossi, A. ; Landrini, M. Numerical simulation of interfacial flows by smoothed particle hydrodynamics. *Journal of Computational Physics*, **191**2: 448–475, 2003.
26. Vila, J. P. On Particle Weighted Methods and Smooth Particle Hydrodynamics. *Mathematical Models and Methods in Applied Sciences*, **09**02: 161–209, 1999.
27. Cole, R. H. Underwater explosions. Princeton Univ. Press, 1984.
28. Oger, G.; Doring, M.; Alessandrini, B.; Ferrant, P. Two-dimensional SPH simulations of wedge water entries. *Journal of Computational Physics*, **213**2: 803–822, 2006.
29. Chiron, L.; de Leffe, M.; Oger, G.; Le Touz, D. Fast and accurate SPH modelling of 3D complex wall boundaries in viscous and non viscous flows. *Computer Physics Communications*, **234**: 93–111, 2018.